Biointerface Research in Applied Chemistry
Open-Access Journal (ISSN: 2069-5837)

Article
Volume 16, Issue 4, 2026, 117
https://doi.org/10.33263/BRIAC164.117

Structure-Based Computational Evaluation and Pharmacokinetic Profiling of Chelator-Functionalized Eugenol and Thymol Derivatives for Predicted Interaction with Bacterial DNA Gyrase

Manos C. Vlasiou [1,*]

[1] Department of Veterinary Medicine, University of Nicosia School of Veterinary Medicine, 2414, Nicosia, Cyprus
* Correspondence: vlasiou.m@unic.ac.cy;

Received: 4.03.2026; Accepted: 28.05.2026; Published: 15.08.2026

Abstract: Computational approaches play an important role in early-stage compound prioritization, enabling, in this way, the evaluation of molecular interaction patterns and pharmacokinetic properties prior to experimental validation. In the present study, two chelator-functionalized derivatives of the natural phenolic compounds eugenol and thymol were synthesized via Mannich-base modification with a diethanolamine moiety and evaluated using an integrated *in silico* workflow focused on bacterial DNA gyrase. Structure-based molecular docking was performed to investigate predicted binding modes and ligand–protein interaction profiles within the catalytic pocket of the enzyme, followed by post-docking structural relaxation and root-mean-square deviation (RMSD)-based pose persistence assessment. Both derivatives exhibited higher predicted interaction energies and more extensive hydrogen-bonding networks than their parent compounds, suggesting enhanced ligand accommodation within the active site. In parallel, *in silico* pharmacokinetic profiling was conducted to assess physicochemical properties, gastrointestinal absorption, and drug-likeness. Both compounds demonstrated favorable predicted ADME profiles and compliance with Lipinski's rule of five. Complementary Density Functional Theory (DFT) calculations further supported the electronic stability of the synthesized derivatives and provided comparative insight into their frontier orbital characteristics and global reactivity descriptors. The findings demonstrate how chelator-guided modification of natural product scaffolds can be explored through integrated computational modeling and pharmacokinetic filtering to support candidate selection for future experimental antibacterial research.

Keywords: *in silico* evaluation; molecular docking; DNA gyrase; eugenol derivatives; thymol derivatives; chelator functionalization; Mannich base derivatives; ADME prediction; computational compound prioritization.

1. Introduction

The global rise of antimicrobial resistance (AMR) represents a major challenge to both veterinary and human medicine, threatening the effectiveness of existing antibacterial therapies and increasing morbidity, mortality, and economic burden worldwide [1–5]. One well-established strategy to address this challenge is to identify new chemical entities that target essential bacterial enzymes. Among these, bacterial DNA gyrase plays a critical role in DNA

replication and transcription and has long been recognized as an antibacterial target due to its absence in higher eukaryotes and its essentiality to bacterial viability [6–11]. Clinically important antibacterial classes, such as fluoroquinolones, exert their activity by inhibiting DNA gyrase and topoisomerase IV; however, resistance to these agents continues to emerge, highlighting the need for alternative scaffolds and binding modes [12–15].

Natural products remain an important source of structurally diverse scaffolds in antibacterial research. Phenolic compounds such as eugenol and thymol, which are major constituents of several essential oils, have been reported to exhibit antimicrobial activity primarily through membrane disruption and interference with bacterial metabolic processes [16–20]. Despite their broad-spectrum activity, the practical application of these compounds is often limited by moderate potency and unfavorable pharmacokinetic properties, motivating efforts to improve their performance through chemical modification.

Chelation-based modification is one approach to enhance molecular interactions with enzyme active sites by increasing hydrogen-bonding capacity and polar surface functionality. In medicinal and bioinorganic chemistry, the introduction of chelating moieties has been explored as a strategy to modulate target engagement and physicochemical behavior [21–24]. The Mannich reaction is a well-established synthetic method for the functionalization of phenolic compounds, enabling the introduction of aminomethyl groups under mild conditions and providing access to structurally diverse derivatives with altered biological and pharmacokinetic properties [25–29].

Structure-based computational methods, including molecular docking and post-docking analysis, are widely used in early-stage compound prioritization to explore ligand–protein interactions and to guide experimental efforts [30–33]. When combined with *in silico* pharmacokinetic prediction tools, such approaches can help filter compounds based on drug-likeness and absorption-related properties before experimental validation [34–36]. While these methods do not replace biological testing, they provide a rational framework for hypothesis generation and candidate selection in antibacterial research [37,38].

In the present study, an integrated *in silico* drug discovery strategy was employed to investigate two novel chelator-functionalized derivatives of the natural phenolic compounds eugenol and thymol as potential inhibitors of bacterial DNA gyrase. Structural modification was achieved *via* Mannich-base functionalization with a diethanolamine moiety, thereby introducing chelating functionality to enhance interactions within the enzyme's catalytic pocket. Structure-based molecular docking was used to predict binding modes, interaction profiles, and relative binding affinities of the derivatives compared with their parent compounds, followed by a post-docking stability assessment using molecular dynamics–based RMSD analysis. In parallel, *in silico* ADME profiling was conducted to evaluate pharmacokinetic suitability and drug-likeness. This work aims to demonstrate a rational strategy for enhancing the target engagement of natural product scaffolds and to provide a prioritization framework for developing novel antibacterial leads for both veterinary and biomedical applications.

The work is intended as a structure-based computational prioritization and pharmacokinetic filtering exercise rather than as a demonstration of antibacterial efficacy. Molecular docking and post-docking stability analysis are employed to explore ligand–protein interaction patterns and binding-pose persistence within the enzyme’s active site, while *in silico* ADME prediction is used to assess drug-likeness and oral bioavailability. No experimental

enzyme inhibition, antibacterial activity, or *in vivo* validation is reported, and therefore, the findings should be interpreted as hypothesis-generating.

2. Materials and Methods

2.1. Materials and instrumentation.

All reagents and solvents were purchased from Merck (Darmstadt, Germany) and used as received without further purification. ^{1}H NMR spectra were recorded on a Bruker Avance 300 MHz spectrometer at ambient temperature (298 K) using DMSO-d_6 as solvent. Chemical shifts (δ) are reported in parts per million (ppm) relative to tetramethylsilane (TMS) as the internal standard. UV–visible absorption spectra were recorded using a JASCO V-730 UV–Vis spectrophotometer (Tokyo, Japan) over the wavelength range of 200–400 nm, employing 1 cm quartz cuvettes. Samples were prepared in DMSO at concentrations of approximately 1 × 10^{-4} M, unless otherwise stated. Fourier-transform infrared (FTIR) spectra were acquired using a JASCO FT/IR-6600 spectrometer (Tokyo, Japan) in the range of 4000–400 cm^{-1}, using the crystal method. Elemental analyses (C, H, N) were performed using a Vario EL III elemental analyzer (Elementar, Germany). The measured elemental compositions were within ±0.4% of the calculated theoretical values, supporting the proposed molecular formulas. To ensure analytical transparency, the original ^{1}H NMR and FTIR spectra of compounds L1 and L2 are provided in the Supplementary Materials. Elemental analysis is reported as supportive compositional evidence.

2.2. Synthesis of 2,2'-((2-allyl-5-hydroxy-4-methoxybenzyl)azanediyl)diethanol (L1).

The eugenol-derived Mannich base L1 was synthesized using a standard Mannich reaction protocol. Briefly, 4-allyl-2-methoxyphenol (0.5 mmol, 82.1 mg) was dissolved in methanol and refluxed with equimolar amounts of paraformaldehyde (0.5 mmol, 15.0 mg) and diethanolamine (0.5 mmol, 52.6 mg; approximately 48 µL) in the presence of a catalytic amount of sulfuric acid (1–2 drops). The reaction mixture was refluxed for 24 h and monitored by thin-layer chromatography (TLC). Upon completion, the solvent was removed under reduced pressure, yielding a brownish oily residue; isolated yield: 82 %.

^{1}H NMR (300 MHz, DMSO-d_6, δ ppm): 2.50 (m, CH_2–N), 3.21 (m, N–CH_2), 3.65 (br s, OH), 3.83 (s, OCH_3, 3H), 4.48–5.00 (m, CH_2=CH–), 5.35 (s, Ar–OH, 1H), 7.00 (s, aromatic proton, 1H). UV–Vis (λmax, nm): 220, 260, 320. FTIR (cm^{-1}): ~3700 (br, O–H stretch), 2893 (C–H stretch), 1250 (C–N stretch), 1210 (C–O stretch), 947 (C=C vibration), 810 (aromatic C–H bending). Molecular formula: $C_{15}H_{23}NO_4$. Elemental analysis calculated (%): C 64.03, H 8.24, N 4.98. Found (%): C 64.00, H 8.25, N 5.00.

The combined spectroscopic profile, including characteristic aminomethyl-region proton signals, aromatic hydroxyl resonance, and C–N stretching vibration, is consistent with Mannich-base functionalization of the eugenol scaffold. Elemental analysis further supported the proposed molecular composition. Original ^{1}H NMR and FTIR spectra are provided in the Supplementary Materials.

2.3. Synthesis of 2,2'-((4-hydroxy-5-isopropyl-2 methylbenzyl)azanediyl)diethanol (L2).

The thymol-derived Mannich base L2 was synthesized following the same procedure as described for L1. Briefly, 5-methyl-2-(propan-2-yl)phenol (0.5 mmol, 75.1 mg) was reacted

with equimolar amounts of paraformaldehyde (0.5 mmol, 15.0 mg) and diethanolamine (0.5 mmol, 52.6 mg; approximately 48 µL) in methanol under reflux for 24 h in the presence of catalytic sulfuric acid. Reaction progress was monitored by TLC. The solvent was removed under reduced pressure to afford the final product; isolated yield: 79%.

^{1}H NMR (300 MHz, DMSO-d_6, δ ppm): 1.20 (d/m, CH_3), 2.34 (m, aromatic CH_3), 2.53 (m, CH_2–N), 3.05 (m, CH), 3.45 (m, N–CH_2), 3.65 (br s, OH), 5.35 (s, Ar–OH, 1H), 6.77 (s, aromatic proton, 1H), 6.88 (s, aromatic proton, 1H). UV–Vis (λmax, nm): 220. FTIR (cm^{-1}): ~3668 (br, O–H stretch), 2893 (C–H stretch), 1250 (C–N stretch), 1150 (C–O stretch), 947 (C=C vibration), 810 (aromatic C–H bending). Molecular formula: $C_{15}H_{25}NO_3$. Molecular weight: 267.36 g/mol. Elemental analysis calculated (%): C 67.38, H 9.42, N 5.24. Found (%): C 67.35, H 9.40, N 5.27.

The observed spectroscopic features support the successful Mannich-base functionalization of the thymol scaffold by introducing the diethanolamine moiety. The appearance of characteristic aminomethyl-region resonances and C–N stretching vibrations, together with agreement with elemental analysis, supports the proposed substitution pattern. Original ^{1}H NMR and FTIR spectra are included in the Supplementary Materials.

2.4. Molecular docking studies.

Structure-based molecular docking was performed to evaluate the predicted binding modes and relative interaction energies of the synthesized ligands (L1 and L2) with bacterial DNA gyrase. The X-ray crystal structure used for docking was PDB ID: 4URO, corresponding to the ATPase domain of the DNA gyrase B (GyrB) subunit from Staphylococcus aureus. Chain A of the crystallographic structure was used for all docking calculations. The crystal structure contains a co-crystallized ATPase-site inhibitor bound within the catalytic ATP-binding pocket, which was used to define the docking region and validate the docking protocol [39].

DNA gyrase is a type II bacterial topoisomerase responsible for ATP-dependent negative supercoiling of DNA and is essential for bacterial DNA replication and transcription. The ATP-binding region of the GyrB subunit represents a well-established antibacterial target and has been exploited by several classes of antibacterial agents and experimental gyrase inhibitors [40]. The 4URO structure was selected because it provides a well-resolved inhibitor-bound conformation of the ATPase catalytic domain, suitable for structure-based docking and comparative ligand-interaction analysis.

Docking calculations were therefore focused specifically on the experimentally characterized ATP-binding catalytic pocket identified by the position of the co-crystallized ligand within the crystal structure. This targeted docking approach was adopted to improve biological relevance and ensure that predicted ligand poses were generated within a validated inhibitor-binding region associated with DNA gyrase catalytic activity [41,42]. The present computational workflow was intended to investigate predicted ligand–protein interaction patterns and comparative docking behavior within this experimentally resolved catalytic site rather than to demonstrate experimentally confirmed DNA gyrase inhibition or antibacterial activity.

2.4.1. Protein preparation.

The protein structure was prepared using standard preprocessing protocols. All crystallographic water molecules, buffer components, and non-essential heteroatoms were

removed. The co-crystallized ligand was removed prior to docking calculations, and its binding site coordinates were retained for defining the docking region. Polar hydrogen atoms were added, and protonation states of ionizable residues were assigned, assuming physiological pH (7.4). No additional energy minimization of the protein backbone was performed in order to preserve the experimentally determined crystallographic conformation. The prepared protein structure was saved in PDB format for subsequent docking calculations [43].

2.4.2. Ligand preparation.

Three-dimensional structures of L1 and L2 were constructed and geometry-optimized using the semi-empirical PM3 method to obtain low-energy conformations prior to docking. The optimized geometries were converted into the format required for docking simulations. All rotatable bonds were defined as flexible during docking, allowing conformational sampling of ligand flexibility within the binding site.

2.4.3. Docking protocol.

Molecular docking simulations were performed using the iGEMDOCK software package, which employs a genetic algorithm–based conformational search strategy combined with an empirical scoring function that incorporates van der Waals, hydrogen-bonding, and electrostatic interaction terms. Docking calculations were conducted using the following parameters:

- Population size: 300
- Generations: 80
- Number of solutions per ligand: 10
- Default scoring function parameters

Docking was performed using a targeted approach focused on the known catalytic pocket of DNA gyrase, defined based on the coordinates of the co-crystallized ligand in the 4URO structure. This strategy was adopted to ensure the generation of biologically relevant poses within the validated inhibitor-binding region [44]. For each ligand, the pose with the lowest total docking energy located within the catalytic pocket was selected for further analysis. Binding affinity was expressed as total docking energy (kJ/mol), as calculated by the iGEMDOCK scoring function. It is emphasized that these values represent relative interaction energies and should not be interpreted as experimental binding free energies.

2.4.4. Post-docking structural refinement and stability assessment.

To evaluate whether the predicted docking poses remained structurally consistent after local relaxation, post-docking structural refinement was performed using YASARA. Ligand–protein complexes were subjected to short energy minimization and local molecular mechanics relaxation under standard force-field conditions. Root-mean-square deviation (RMSD) values were subsequently calculated for ligand heavy atoms relative to the initial docked conformations [45].

RMSD analysis was used as a qualitative indicator of pose persistence within the ATP-binding catalytic pocket following local structural adjustment. The procedure was intended to evaluate the stability of the predicted docking orientation after energy minimization rather than to provide quantitative thermodynamic or kinetic binding information.

Importantly, no extended time-resolved molecular dynamics (MD) simulations were performed in the present study. Accordingly, the reported analysis should not be interpreted as a full molecular dynamics simulation or trajectory-based conformational sampling. In addition, free-energy calculations such as MM-PBSA or MM-GBSA were not conducted. The present workflow was therefore limited to post-docking structural refinement and qualitative assessment of pose persistence within the experimentally defined catalytic region [46].

2.4.5. Docking protocol validation.

To assess the reliability and reproducibility of the docking protocol, a redocking validation procedure was performed using the co-crystallized ligand originally present in the ATP-binding catalytic pocket of the 4URO DNA gyrase structure. The native ligand was extracted from the crystallographic complex and subsequently re-docked into the same binding region using identical docking parameters, scoring settings, and search conditions applied to ligands L1 and L2.

Validation quality was assessed by comparing the predicted redocked pose with the experimentally resolved crystallographic conformation. Root-mean-square deviation (RMSD) values were calculated using heavy atoms of the ligand after optimal spatial superposition of the crystallographic and predicted conformations. An RMSD threshold ≤ 2.0 Å is commonly accepted as indicative of satisfactory reproduction of the experimental binding mode in molecular docking validation studies [47]. In the present study, the redocking procedure produced an RMSD value of 1.8 Å, supporting the ability of the selected docking protocol to reproduce biologically relevant ligand orientations within the catalytic ATP-binding pocket.

Visual overlay analysis of the crystallographic and redocked conformations demonstrated close spatial agreement between the experimentally observed and computationally predicted ligand poses. In addition, the redocked ligand reproduced key interaction patterns observed in the crystal structure, including hydrogen-bonding and hydrophobic interactions within the ATPase catalytic region of the GyrB subunit. These findings support the suitability of the selected docking parameters for comparative interaction analysis of the synthesized derivatives.

2.4.6. Interaction analysis.

Hydrogen-bond interactions were further evaluated by measuring donor–acceptor distances within the predicted ligand–protein complexes. For L1, the principal hydrogen-bond interactions with ASN54, ASP81, GLY85, SER128, and THR173 were associated with predicted donor–acceptor distances ranging from approximately 2.6 to 3.3 Å, consistent with geometrically favorable hydrogen-bond formation within the ATP-binding catalytic pocket. Similarly, L2 exhibited hydrogen-bond interactions with GLY85, ILE86, and ARG144, with predicted distances of approximately 2.8-3.4 Å. Following post-docking structural refinement and local molecular mechanics relaxation, the principal interaction patterns observed in the initial docking poses remained largely preserved. The major hydrogen-bond contacts identified during docking persisted after local structural adjustment, supporting the qualitative persistence of the pose within the catalytic region. No major displacement of the ligands outside the ATP-binding pocket was observed during the refinement procedure.

The interaction persistence analysis performed in the present study was limited to post-docking local relaxation and RMSD-based structural assessment. Extended time-resolved

molecular dynamics simulations, consensus docking using multiple docking engines, and free-energy calculations were not performed. Therefore, dynamic conformational behavior and quantitative binding energetics could not be evaluated. These approaches would provide valuable additional validation and represent important directions for future investigation.

2.5. In silico ADMET prediction.

In silico absorption, distribution, metabolism, and excretion (ADME) properties of the synthesized compounds were predicted using the SwissADME online platform (https://www.swissadme.ch). SMILES representations of the optimized ligand structures were used as input for the calculations. Predicted parameters included lipophilicity (logP), aqueous solubility (logS), gastrointestinal absorption, blood–brain barrier permeability, cytochrome P450 inhibition profiles, and compliance with Lipinski's rule of five. Toxicological risk was inferred indirectly using pharmacokinetic descriptors, as SwissADME does not provide comprehensive toxicity predictions. Additional toxicological data were retrieved using the pkCSM software and Toxtree. The ADME results were used as a preliminary filter to assess drug-likeness and translational suitability of the proposed DNA gyrase inhibitors.

2.6. Density functional theory (DFT) calculations.

Quantum chemical calculations were performed to investigate the electronic properties of the synthesized ligands L1 and L2 and to derive global reactivity descriptors relevant to their interaction potential. All calculations were conducted using Density Functional Theory (DFT) as implemented in ORCA 5.0. Geometry optimizations were carried out in the gas phase using the B3LYP exchange–correlation functional in combination with the 6-31G(d,p) basis set. No symmetry constraints were applied during optimization. Frequency calculations were subsequently performed at the same level of theory to confirm that the optimized geometries corresponded to true minima on the potential energy surface (no imaginary frequencies detected). Frontier molecular orbital energies (HOMO and LUMO) were extracted from the optimized structures. Based on Koopmans-type approximations, the following global conceptual DFT descriptors were calculated:

- Ionization potential (IP) ≈ −E_HOMO
- Electron affinity (EA) ≈ −E_LUMO
- Chemical potential (μ) = $\frac{(E_{HOMO}+ E_{LUMO})}{2}$
- Electronegativity (χ) = −μ
- Global hardness (η) = $\frac{(E_{LUMO}- E_{HOMO})}{2}$
- Global softness (S) = $\frac{1}{n}$
- Electrophilicity index (ω) = $\frac{\mu^{2}}{2n}$

All orbital energies are reported in electron volts (eV). The calculated descriptors were used to qualitatively compare electronic stability, reactivity, and potential interaction characteristics between L1 and L2. It is noted that these global descriptors provide theoretical approximations derived from gas-phase calculations and do not directly correspond to experimental thermodynamic quantities.

3. Results and Discussion

3.1. Chemistry and structure.

2,2'-((2-allyl-5-hydroxy-4-methoxybenzyl)azanediyl)diethanol (L1) and 2,2'-((4-hydroxy-5-isopropyl-2-methyl benzyl)azanediyl)diethanol (L2) were synthesized based on the Mannich reaction of a secondary amine, diethanolamine. The synthetic procedure can be found in Figure 1 for L1 and Figure 2 for L2. The reactions lasted for 24 hours after adding H_2SO_4 to catalyze the reaction. The optimized structures of L1 and L2 can be found in Figure 3.

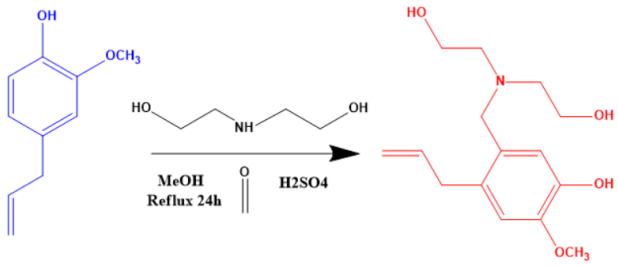

Figure 1. Synthetic route for the preparation of 2,2′-((2-allyl-5-hydroxy-4-methoxybenzyl)azanediyl)diethanol (L1) via Mannich-base functionalization of eugenol using diethanolamine and paraformaldehyde under acidic conditions.

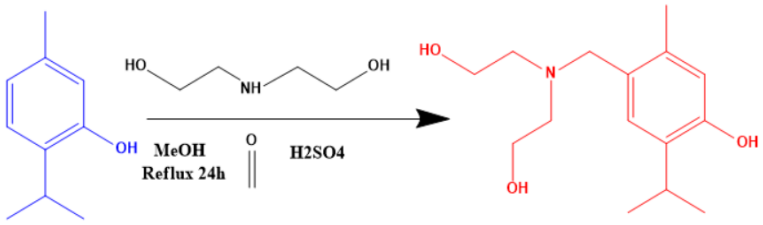

Figure 2. Synthetic route for the preparation of 2,2′-((4-hydroxy-5-isopropyl-2 methylbenzyl)azanediyl)diethanol (L2) via Mannich-base functionalization of thymol using diethanolamine and paraformaldehyde under acidic conditions.

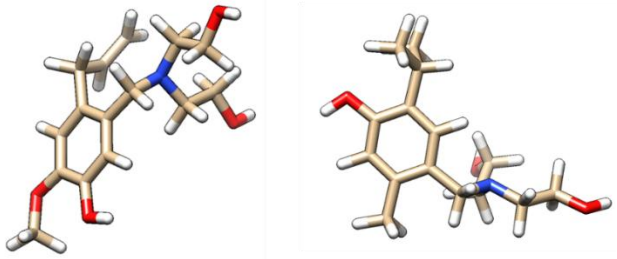

Figure 3. Three-dimensional optimized molecular structures of the synthesized chelator derivatives: L1 (left) and L2 (right), highlighting the diethanolamine moiety introduced through Mannich functionalization.

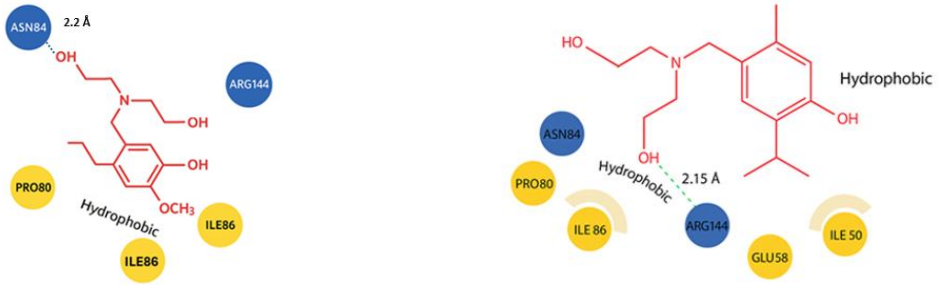

(a) **(b)**

Figure 4. Two-dimensional representations of the binding interactions between the synthesized ligands and the active site of bacterial DNA gyrase (PDB ID: 4URO): **(a)** L1; **(b)** L2. Hydrogen bonds are shown as dashed lines, and key interacting amino acid residues are indicated.

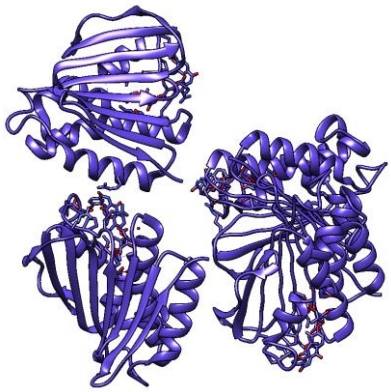

Figure 5. DNA gyrase (PDB ID: 4URO)

3.2. Molecular docking studies on DNA gyrase.

Structure-based molecular docking was performed to investigate the interaction of the chelator-functionalized eugenol (L1) and thymol (L2) derivatives with bacterial DNA gyrase (PDB ID: 4URO) and to rationalize their predicted interaction with DNA gyrase at the molecular level (Figure 5). DNA gyrase is a well-established antibacterial target that catalyzes ATP-dependent negative supercoiling of DNA, a process essential for bacterial replication and transcription. Inhibition of this enzyme has been clinically validated through several antibiotic classes, making it a suitable model system for early-stage *in silico* screening.

The docking results indicated that both derivatives are favorably accommodated within the active-site pocket of DNA gyrase, exhibiting higher predicted binding affinity than their parent compounds. As summarized in Table 1, L1 displayed a binding energy of −84.37 kJ/mol, whereas L2 exhibited a binding energy of −75.06 kJ/mol. For comparison, the parent phenolic compounds eugenol and thymol showed lower predicted affinities (−73.61 and −66.50 kJ/mol, respectively), suggesting that Mannich-base functionalization with a diethanolamine moiety significantly enhances enzyme–ligand interactions (Figure 4). Detailed analysis of the binding modes revealed that L1 forms five hydrogen bonds with key residues within the gyrase active site, namely ASN54, ASP81, GLY85, SER128, and THR173. These interactions are complemented by stabilizing van der Waals contacts involving ASN54, GLU58, and ILE82. Several of these residues are located within or proximal to the catalytic pocket and have been reported to participate in ligand recognition in known DNA gyrase inhibitors. The higher number and spatial distribution of hydrogen bonds formed by L1 likely contribute to its superior binding affinity and more stable anchoring within the active site.

In contrast, L2 formed three hydrogen bonds with GLY85, ILE86, and ARG144, accompanied by van der Waals interactions with ASN54, GLU58, ARG84, ILE86, and PRO87. Although these interactions remain indicative of favorable binding, the reduced hydrogen-bonding network compared with L1 may account for L2's lower predicted affinity. Structurally, this difference can be attributed to variations in substituent bulk and flexibility between the two ligands, which influence their orientation and accommodation within the binding pocket. Importantly, the introduction of the diethanolamine chelating group appears to be critical for enhancing ligand–protein interactions. Beyond increasing hydrogen-bonding capacity, the chelating moiety may facilitate additional electrostatic stabilization and improve ligand positioning within the DNA gyrase active site through enhanced hydrogen bonding and polar interactions. This chelation-assisted anchoring effect provides a plausible mechanistic explanation for the observed improvement in binding affinity relative to the parent essential oil

compounds. Post-docking relaxation and RMSD analysis indicated that both ligand–protein complexes retained their binding orientation following local structural adjustment, suggesting persistence of the predicted docking poses within the DNA gyrase active site.

It should be emphasized that consensus docking using multiple docking engines and extended molecular dynamics simulations was not performed in the present study, and experimental validation will be required to evaluate these observations further.

Overall, these findings demonstrate that chelation-guided modification of natural product scaffolds can enhance target engagement at the molecular level and underscore the value of molecular docking as a prioritization tool in antibacterial drug discovery pipelines.

Table 1. Comparative molecular docking results of chelator-functionalized derivatives (L1 and L2), parent compounds (eugenol and thymol), and the co-crystallized reference DNA gyrase inhibitor against the ATP-binding catalytic pocket of bacterial DNA gyrase (PDB ID: 4URO). Predicted interaction energies, hydrogen-bond interactions, and major van der Waals contacts are shown for all compounds using the same docking protocol.

Compound	Predicted interaction energy (kJ/mol)	Hydrogen-bond interactions	Major van der Waals contacts
Eugenol	−73.61	ASN54, GLY85	GLU58, ILE82
Thymol	−66.50	GLY85	ASN54, PRO87
L1	−84.37	ASN54, ASP81, GLY85, SER128, THR173	ASN54, GLU58, ILE82
L2	−75.06	GLY85, ILE86, ARG144	ASN54, GLU58, ARG84, ILE86, PRO87
Co-crystallized inhibitor	-92.14	ASP81, GLY85, ARG84, THR173	ASN54, ILE82, PRO87, VAL120

The reference inhibitor novobiocin reproduced the expected interaction profile within the ATP-binding catalytic region of the GyrB subunit, supporting the biological relevance of the selected docking pocket and enabling comparative interpretation of the synthesized derivatives relative to a crystallographically characterized DNA gyrase ligand.

3.2.1. Interaction energy component analysis.

To further rationalize the differences in predicted binding energies between L1, L2, and their parent scaffolds, the individual energy contributions provided by the iGEMDOCK scoring function were examined. The total docking score represents a composite of van der Waals, hydrogen bonding, and electrostatic interaction terms, allowing qualitative dissection of the dominant stabilizing forces within the catalytic pocket.

For L1, the enhanced total docking energy was primarily driven by an increased hydrogen-bonding contribution relative to eugenol, consistent with the formation of five stabilizing hydrogen bonds within the active site. The introduction of the diethanolamine moiety substantially increases the number of polar functional groups capable of acting as hydrogen-bond donors and acceptors. This modification appears to strengthen polar anchoring within the ATP-binding region, thereby lowering the overall docking energy. In addition, van der Waals interactions between the aromatic scaffold and hydrophobic residues lining the pocket contribute to shape complementarity and dispersion stabilization. In contrast, L2 showed a smaller improvement in total docking energy compared with thymol, reflecting a more modest increase in hydrogen-bonding interactions. Although the chelating substituent introduces additional polar functionality, its spatial orientation within the binding pocket is less optimal than that of L1, resulting in fewer high-quality hydrogen bonds. The van der Waals contribution for L2 remains comparable to that of L1, suggesting that the primary

differentiating factor between the two derivatives lies in polar interaction efficiency rather than hydrophobic complementarity.

From a medicinal chemistry perspective, these observations highlight the importance of the balance of interactions within enzyme active sites. While hydrophobic contacts contribute to baseline binding affinity, strategic enhancement of directional hydrogen bonding within key catalytic residues often provides greater gains in interaction energy. The data suggest that in the present series, hydrogen-bond optimization via chelator-functionalization is the principal driver of improved predicted binding affinity, particularly in the eugenol-derived analog. It is important to note that the interaction energy components reported by empirical scoring functions are approximations and do not directly correspond to experimentally measurable thermodynamic parameters.

3.3. ADME studies.

In silico assessment of absorption, distribution, metabolism, and excretion (ADME) properties represents a critical step in early-stage drug discovery, as unfavorable pharmacokinetic profiles are a common cause of late-stage attrition. To evaluate the drug-likeness and translational suitability of the proposed DNA gyrase inhibitors, ADME prediction was performed using the SwissADME platform, with the results summarized in Table 2. Both chelator derivatives exhibited favorable physicochemical properties and complied fully with Lipinski's rule of five, indicating good oral drug-likeness. Specifically, neither compound exceeded the recommended thresholds for molecular weight, hydrogen bond donors or acceptors, nor lipophilicity, suggesting an appropriate balance between polarity and membrane permeability. The predicted logP values for L1 (2.22) and L2 (2.70) fall within the optimal range for oral bioavailability, supporting efficient gastrointestinal absorption without excessive hydrophobicity. Consistent with these physicochemical parameters, both compounds were predicted to exhibit high gastrointestinal absorption. This feature is particularly relevant for potential oral administration in veterinary and biomedical applications, where ease of dosing and systemic exposure are essential considerations. The predicted aqueous solubility (logS values of −2.22 for L1 and −2.47 for L2) further supports sufficient solubility for oral formulations while remaining compatible with membrane permeability.

Notably, differences in blood–brain barrier (BBB) permeability were observed between the two derivatives. L1 was predicted to be BBB-permeant, whereas L2 was not. From a safety perspective, limited central nervous system penetration is often desirable for antibacterial agents intended for systemic use, as it may reduce the risk of neurotoxicity and off-target effects. In this context, the lack of predicted BBB permeability for L2 may represent an advantage for certain therapeutic applications, particularly in food-producing animals. Conversely, BBB penetration by L1 may warrant further consideration depending on the intended indication and dosing regimen.

Metabolic liability was also assessed through cytochrome P450 (CYP) inhibition profiling. Neither compound was predicted to inhibit major CYP isoforms, including CYP1A2, CYP2C9, CYP2C19, CYP2D6, and CYP3A4, suggesting a low likelihood of clinically relevant drug–drug interactions. This profile is favorable for further development, especially in veterinary settings where polypharmacy is common.

Taken together, the ADME predictions indicate that both chelator-functionalized derivatives possess drug-like characteristics compatible with oral administration and systemic exposure. While *in silico* ADME modeling cannot fully substitute for experimental

pharmacokinetic studies, these results provide an important preliminary filter that supports prioritizing L1 and L2 as candidate compounds for further biological evaluation. Moreover, the combination of favorable predicted pharmacokinetics with enhanced target binding underscores the utility of integrated computational screening approaches in antibacterial drug discovery.

Although both synthesized derivatives demonstrated favorable predicted physicochemical properties and compliance with Lipinski's rule of five, such descriptors alone are insufficient to predict antibacterial efficacy, particularly against Gram-negative organisms. Antibacterial activity is strongly influenced by additional factors, including outer membrane permeability, active efflux systems, porin-mediated transport, and intracellular accumulation, which conventional drug-likeness models do not fully capture. Gram-negative bacteria possess an additional outer membrane enriched in lipopolysaccharides that can substantially restrict penetration of moderately lipophilic compounds and larger polar molecules. Furthermore, multidrug efflux pumps may actively reduce intracellular accumulation of antibacterial agents even when favorable docking interactions are predicted. In contrast, Gram-positive organisms generally lack the outer membrane permeability barrier, potentially allowing improved access of small molecules to intracellular targets such as DNA gyrase.

The presence of the diethanolamine-containing chelator moiety in L1 and L2 increases polarity and hydrogen-bonding capacity, which may influence permeability and intracellular distribution differently across bacterial classes. While these structural characteristics may support interaction with the ATP-binding catalytic pocket of DNA gyrase, their influence on bacterial susceptibility to uptake and efflux remains unknown and would require experimental investigation.

Thus, the present computational findings should be interpreted with caution and primarily as a structure-based prioritization exercise rather than as a prediction of confirmed antibacterial activity against either Gram-positive or Gram-negative pathogens. Future studies incorporating permeability assays, bacterial accumulation measurements, efflux evaluation, and minimum inhibitory concentration (MIC) testing across representative bacterial species will be necessary to establish the translational relevance of these compounds.

Table 2. *In silico* ADME properties of the synthesized compounds L1 and L2 predicted using the SwissADME platform, including physicochemical parameters, absorption characteristics, blood–brain barrier permeability, cytochrome P450 inhibition profiles, and Lipinski's rule of five compliance.

Substance	**L1**	**L2**
Log P	2.22	2.70
Log S	-2.22	-2.47
GI absorption	High	High
BBB permeant	Yes	No
CYP1A2 inhibitor	No	No
CYP2C19 inhibitor	No	No
CYP2C9 inhibitor	No	No
CYP2D6 inhibitor	No	No
CYP3A4 inhibitor	No	No
Log K	-6.57 cm/s	-6.60 cm/s
Lipinski	Yes	Yes

The spectroscopic characterization revealed the addition of the chelating diethanolamine agent in both cases. ^{1}NMR showed a 5.35 (s, -OH aromatic) chemical shift, confirming the substitution. Additionally, IR spectroscopy provided a robust, broad signal revealing the -OH groups of the new molecules and, at 1250 cm ^{1} (m, -C-N amine stretch), also confirms the substitution. The specific molecular formula has been determined by elemental

analysis. The molecular docking analysis showed that the eugenol derivative L1 has a higher binding affinity for DNA gyrase. Additionally, the same happens with the thymol case. The thymol derivative L2 has a higher binding affinity to the protein than the thymol molecule. Predicting a drug's fate and the effects it causes in the body, such as how much is absorbed when administered orally and how much is absorbed in the gastrointestinal tract, is also of the utmost importance. Similarly, if absorption is poor, its distribution and metabolism would be affected, potentially leading to neurotoxicity and nephrotoxicity. Both substances obey Lipinski's rule for oral drugs.

3.4. In silico toxicity assessment and comparative safety profile.

The *in silico* toxicity profiles of L1 and L2 are summarised in Table 3. Both compounds were predicted to be non-mutagenic, as indicated by negative AMES toxicity results. Neither compound showed predicted inhibition of hERG I or hERG II potassium channels, suggesting a low risk of cardiotoxicity associated with QT interval prolongation. Acute oral toxicity predictions in rats indicated low acute toxicity for both compounds, with LD_{50} values of 2.312 mol/kg for L1 and 2.343 mol/kg for L2. Chronic toxicity modeling predicted lowest observed adverse effect levels (LOAELs) of 1.526 log mg/kg_bw/day for L1 and 1.197 log mg/kg_bw/day for L2, indicating that L1 may exhibit a slightly higher threshold for chronic adverse effects. The predicted maximum tolerated human dose was marginally higher for L2 (0.217 log mg/kg/day) compared to L1 (0.171 log mg/kg/day).

Neither compound was predicted to induce hepatotoxicity or skin sensitization. Environmental toxicity predictions indicated moderate protozoal toxicity toward *Tetrahymena pyriformis*, with slightly lower predicted toxicity for L2 (0.198 log µg/L) than for L1 (0.276 log µg/L). Minnow toxicity predictions indicated low to moderate fish toxicity for both compounds, with L1 showing a higher tolerance value (2.22 log mM) than L2 (1.757 log mM). Both compounds demonstrated favorable *in silico* safety profiles, successfully clearing key early-stage toxicity liabilities, including genotoxicity, cardiotoxicity, hepatotoxicity, and skin sensitization. The absence of predicted AMES mutagenicity and hERG channel inhibition is particularly important, as these endpoints represent common causes of late-stage attrition in drug development and are critical considerations in regulatory toxicology.

The predicted acute toxicity values indicate low risk following single-dose oral exposure for both compounds. Notably, the LD_{50} values are comparable, suggesting no substantial difference in acute toxicity potential. However, differences emerge under chronic exposure modeling. L1 exhibited a higher predicted LOAEL than L2, implying a wider safety margin during prolonged exposure. This distinction may be relevant in veterinary or food-chain-related applications, where repeated administration or long-term exposure is anticipated.

Conversely, L2 showed a higher predicted maximum tolerated human dose, suggesting marginally improved systemic tolerability under controlled dosing conditions. This observation may reflect subtle differences in predicted absorption, distribution, or metabolic handling between the two compounds, although experimental pharmacokinetic validation would be required to confirm this hypothesis. From an environmental perspective, both compounds exhibited moderate protozoal toxicity and low-to-moderate fish toxicity, consistent with those of biologically active small molecules. L2 demonstrated slightly lower protozoal toxicity, whereas L1 exhibited lower predicted fish toxicity, indicating that neither compound presents a clearly dominant environmental safety advantage at this stage.

Overall, the comparative *in silico* toxicity assessment suggests that both compounds have acceptable, largely comparable safety profiles, with L1 exhibiting a potentially more favorable chronic exposure margin and L2 showing slightly improved systemic tolerability. These results support advancing both candidates to targeted experimental validation, in which *in vitro* cytotoxicity assays and, if required, focused *in vivo* studies can further refine safety margins and guide compound prioritization, depending on the intended veterinary, translational, or food-safety application.

Table 3. Comparative *in silico* toxicity profiles of L1 and L2 compounds.

Toxicological endpoint	L1	L2	Unit/model output	Comparative interpretation
AMES toxicity	No	No	Categorical (Yes/No)	Both compounds predicted non-mutagenic
Max. tolerated dose (human)	0.171	0.217	log mg/kg/day	Slightly higher tolerability predicted for L2
hERG I inhibition	No	No	Categorical (Yes/No)	No predicted cardiotoxic liability
hERG II inhibition	No	No	Categorical (Yes/No)	No predicted cardiotoxic liability
Oral rat acute toxicity (LD_{50})	2.312	2.343	mol/kg	Comparable low acute oral toxicity
Oral rat chronic toxicity (LOAEL)	1.526	1.197	log mg/kg_bw/day	Higher chronic safety margin for L1
Hepatotoxicity	No	No	Categorical (Yes/No)	No predicted liver toxicity
Skin sensitisation	No	No	Categorical (Yes/No)	Low occupational exposure risk
Tetrahymena pyriformis toxicity	0.276	0.198	log µg/L	Slightly lower protozoal toxicity for L2
Minnow toxicity	2.22	1.757	log mM	Lower predicted fish toxicity for L1

All values represent in silico predictions generated using validated machine-learning toxicity models. Lower LD_{50} and LOAEL values indicate greater toxicity, whereas higher maximum tolerated doses indicate greater predicted systemic tolerability. Environmental toxicity endpoints reflect estimated aquatic organism sensitivity and are intended for preliminary screening only.

3.5. Density functional theory (DFT) analysis of electronic properties.

To complement the structure-based docking analysis and provide additional insight into the electronic characteristics of the chelator-functionalized derivatives, Density Functional Theory (DFT) calculations were performed at the B3LYP/6-31G(d) level using ORCA. The optimized geometries corresponded to true minima on the potential energy surface, as confirmed by the absence of imaginary frequencies.

3.5.1. Frontier molecular orbital analysis.

The calculated frontier molecular orbital energies are summarized in Table 4.

- **L1:** HOMO = −8.356 eV; LUMO = +0.422 eV
- **L2:** HOMO = −9.247 eV; LUMO = −0.148 eV

The HOMO–LUMO energy gap (ΔE) was 8.778 eV for L1 and 9.099 eV for L2. Both compounds, therefore, exhibit relatively large energy gaps, consistent with electronically stable organic scaffolds. The slightly larger ΔE observed for L2 suggests a marginally greater electronic hardness than for L1. In qualitative terms, the HOMO represents the electron-donating capacity of the molecule, while the LUMO reflects its ability to accept electron density. The lower HOMO energy of L2 indicates a reduced tendency toward electron donation relative to L1, whereas the slightly lower LUMO energy suggests improved electron-accepting potential. However, the differences between the two compounds are moderate, and both remain within a range typical for neutral, nonconjugated aromatic systems.

Importantly, the large HOMO–LUMO gaps for both derivatives support the interpretation that their interaction with DNA gyrase is governed primarily by noncovalent forces (hydrogen bonding, electrostatic interactions, and dispersion contributions) rather than intrinsic electronic reactivity (Figure 6).

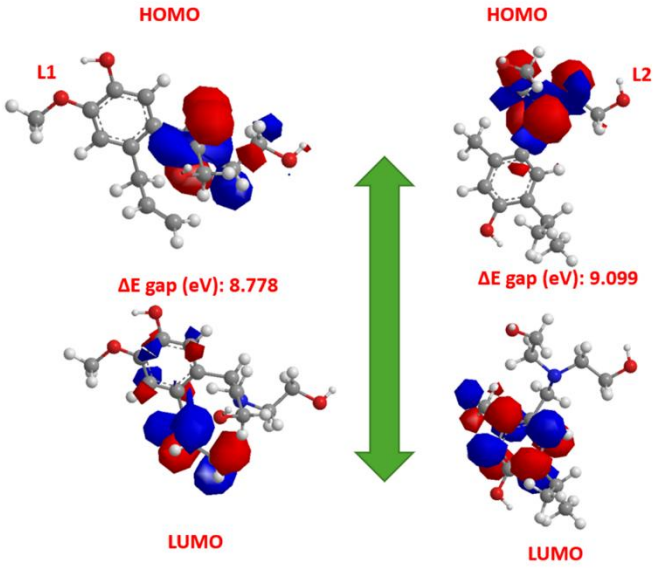

Figure 6. Frontier molecular orbitals and energy gaps of ligands L1 and L2 calculated at the B3LYP/6-31G(d) level using ORCA. Isosurface plots of the highest occupied molecular orbital (HOMO) and lowest unoccupied molecular orbital (LUMO) are shown for each ligand, together with the corresponding HOMO–LUMO energy gap (ΔE). Orbital energies are reported in electron volts (eV).

3.5.2. Global reactivity descriptors.

Global conceptual DFT descriptors were derived from the frontier orbital energies using Koopmans-type approximations (Table 4).

L2 exhibited: Higher ionization potential (9.247 eV vs 8.356 eV for L1); Slightly greater global hardness (η = 4.550 eV vs 4.389 eV for L1); Lower global softness (S = 0.220 vs 0.228 for L1); Higher electrophilicity index (ω = 2.425 eV vs 1.793 eV for L1).

The higher global hardness of L2 is consistent with its slightly larger HOMO–LUMO gap, indicating increased resistance to charge-transfer deformation. Conversely, L1 demonstrates marginally greater softness and a slightly lower ionization potential, suggesting somewhat enhanced electron-donating character.

Table 4. Frontier molecular orbital energies (HOMO, LUMO) and global reactivity descriptors of L1 and L2 calculated at the B3LYP/6-31G(d) level using ORCA. ΔE: HOMO–LUMO energy gap; IP: ionization potential (−E_HOMO); EA: electron affinity (−E_LUMO); μ: chemical potential; χ: electronegativity; η: global hardness; S: global softness; ω: electrophilicity index. Energies are reported in eV. Descriptors were derived using Koopmans-type approximations and are presented for comparative purposes.

Descriptor	L1	L2
HOMO (eV)	−8.356	−9.247
LUMO (eV)	0.422	−0.148
ΔE gap (eV)	8.778	9.099
Ionization Potential, IP (eV)	8.356	9.247
Electron Affinity, EA (eV)	−0.422	0.148
Chemical Potential, μ (eV)	−3.967	−4.698
Electronegativity, χ (eV)	3.967	4.698
Global Hardness, η (eV)	4.389	4.550
Global Softness, S (1/eV)	0.228	0.220
Electrophilicity Index, ω (eV)	1.793	2.425

From a medicinal chemistry perspective, softer molecules may adapt more readily to polar interaction environments through electronic redistribution. This observation may partially rationalize the slightly stronger docking score observed for L1, which formed a more extensive hydrogen-bonding network within the catalytic pocket. However, the electronic differences between the two ligands are subtle and should be interpreted cautiously.

The higher electrophilicity index of L2 indicates a greater theoretical propensity to accept electron density. In the context of protein–ligand interactions, this descriptor may influence interactions with electron-rich residues; however, no evidence for covalent or charge-transfer mechanisms is provided in the present study.

3.5.3. Correlation with docking observations.

When considered alongside the docking results, the DFT analysis suggests that the improved predicted binding affinity of L1 is not driven by greater intrinsic electronic reactivity but rather by geometric and hydrogen-bonding complementarity within the DNA gyrase catalytic pocket. Both derivatives exhibit electronic stability compatible with drug-like scaffolds. The minor differences in softness and ionization potential between L1 and L2 may contribute to subtle variations in interaction adaptability. Still, the dominant determinants of predicted binding appear to be structural orientation and hydrogen-bond network formation rather than frontier orbital energetics. Therefore, the DFT analysis supports the docking findings by confirming that both ligands possess electronically stable frameworks capable of participating in directional noncovalent interactions, without indicating excessive intrinsic reactivity.

3.6. Limitations of the computational study.

The findings of this study are subject to several limitations inherent to computational drug discovery approaches. Molecular docking and post-docking stability analyses provide predictive insights into ligand–protein interactions but do not directly measure biological activity or inhibitory potency. The absence of experimental enzyme inhibition assays, minimum inhibitory concentration (MIC) data, or *in vivo* validation precludes definitive conclusions regarding antibacterial efficacy. In addition, ADME properties were assessed using *in silico* prediction tools, which, while valuable for early-stage screening, cannot fully capture the complexity of absorption, metabolism, and toxicity in biological systems. The results presented herein should be interpreted as a prioritization framework for lead identification rather than as confirmation of therapeutic effectiveness and warrant further experimental validation in future studies.

Docking energies, ADME parameters, toxicity predictions, and DFT-derived descriptors represent computational approximations and should not be interpreted as direct experimental measures of biological activity, pharmacological efficacy, or clinical safety. The computational workflow was limited to single-engine docking and post-docking local structural refinement. Extended molecular dynamics simulations, consensus docking approaches, and trajectory-based free-energy calculations were beyond the scope of the present study and should be considered in future validation studies.

4. Conclusions

In the present study, a unified computational workflow was applied to evaluate chelator-functionalized derivatives of the natural phenolic compounds eugenol and thymol as putative DNA gyrase-binding scaffolds. Structure-based docking analysis indicated that Mannich-base functionalization with a diethanolamine moiety improved predicted ligand–protein interaction patterns and increased the extent of stabilizing hydrogen-bond interactions within the catalytic pocket when compared with the parent compounds. Post-docking structural relaxation further suggested persistence of the predicted binding poses following local energy minimization.

Complementary *in silico* ADME and toxicity profiling suggested favorable predicted physicochemical and pharmacokinetic characteristics, including compliance with Lipinski's rule of five and high predicted gastrointestinal absorption. In addition, Density Functional Theory (DFT) analysis supported the electronic stability of the synthesized derivatives and provided comparative insight into their global reactivity descriptors and frontier molecular orbital properties.

Overall, the present work provides a structure-based computational ranking framework for evaluating chelator-functionalized natural product derivatives in early-stage antibacterial discovery. The results support selecting L1 and L2 as candidates for future experimental investigation. Further studies involving enzyme inhibition assays, antibacterial susceptibility testing, cytotoxicity evaluation, permeability assessment, and extended molecular dynamics simulations will be required to validate the biological relevance and translational potential of these compounds.

Author Contributions

Not applicable.

Institutional Review Board Statement

Not applicable.

Informed Consent Statement

Not applicable.

Data Availability Statement

Data supporting the findings of this study are available upon reasonable request from the corresponding author.

Funding

This research received no external funding.

Acknowledgments

None.

Conflicts of Interest

The authors declare no conflict of interest.

References

1. Levy, S.B.; Marshall, B. Antibacterial resistance worldwide: causes, challenges and responses. *Nat. Med.* **2004**, *10*, S122–S129, https://doi.org/10.1038/nm1145.
2. Jacoby, G.A. ANTIMICROBIAL-RESISTANT PATHOGENS IN THE 1990s. *Annu. Rev. Med.* **1996**, *47*, 169–179, https://doi.org/10.1146/annurev.med.47.1.169.
3. Ventola, C.L. The antibiotic resistance crisis: part 1: causes and threats. *P T* **2015**, *40*, 277-283.
4. Holmes, A.H.; Moore, L.S.P.; Sundsfjord, A.; Steinbakk, M.; Regmi, S.; Karkey, A.; Guerin, P.J.; Piddock, L.J.V. Understanding the mechanisms and drivers of antimicrobial resistance. *Lancet* **2016**, *387*, 176-187, https://doi.org/10.1016/S0140-6736(15)00473-0.
5. Cox, G.; Wright, G.D. Intrinsic antibiotic resistance: Mechanisms, origins, challenges and solutions. *Int. J. Med. Microbiol.* **2013**, *303*, 287–292, https://doi.org/10.1016/j.ijmm.2013.02.009.
6. Drlica, K.; Zhao, X. DNA gyrase, topoisomerase IV, and the 4-quinolones. *Microbiol. Mol. Biol. Rev.* **1997**, *61*, 377–392, https://doi.org/10.1128/MMBR.61.3.377-392.1997.
7. Bush Natassja, G.; Evans-Roberts, K.; Maxwell, A. DNA Topoisomerases. *EcoSal Plus* **2015**, *6*, 10–128, https://doi.org/10.1128/ecosalplus.ESP-0010-2014.
8. Alt, S.; Mitchenall, L.A.; Maxwell, A.; Heide, L. Inhibition of DNA gyrase and DNA topoisomerase IV of *Staphylococcus aureus* and *Escherichia coli* by aminocoumarin antibiotics. *J. Antimicrob. Chemother.* **2011**, *66*, 2061-2069, https://doi.org/10.1093/jac/dkr247.
9. Rajendram, M.; Hurley, K.A.; Foss, M.H.; Thornton, K.M.; Moore, J.T.; Shaw, J.T.; Weibel, D.B. Gyramides Prevent Bacterial Growth by Inhibiting DNA Gyrase and Altering Chromosome Topology. *ACS Chem. Biol.* **2014**, *9*, 1312-1319, https://doi.org/10.1021/cb500154m.
10. Wang, J.C. Cellular roles of DNA topoisomerases: a molecular perspective. *Nat. Rev. Mol. Cell Biol.* **2002**, *3*, 430–440, https://doi.org/10.1038/nrm831.
11. Collin, F.; Karkare, S.; Maxwell, A. Exploiting bacterial DNA gyrase as a drug target: current state and perspectives. *Appl. Microbiol. Biotechnol.* **2011**, *92*, 479–497, https://doi.org/10.1007/s00253-011-3557-z.
12. Marchese, A.; Barbieri, R.; Coppo, E.; Orhan, I.E.; Daglia, M.; Nabavi, S.F.; Izadi, M.; Abdollahi, M.; Nabavi, S.M.; Ajami, M. Antimicrobial activity of eugenol and essential oils containing eugenol: A mechanistic viewpoint. *Crit. Rev. Microbiol.* **2017**, *43*, 668-689, https://doi.org/10.1080/1040841X.2017.1295225.
13. Kamatou, G.P.; Vermaak, I.; Viljoen, A.M. Eugenol—From the Remote Maluku Islands to the International Market Place: A Review of a Remarkable and Versatile Molecule. *Molecules* **2012**, *17*, 6953-6981, https://doi.org/10.3390/molecules17066953.
14. Nostro, A.; Papalia, T. Antimicrobial Activity of Carvacrol: Current Progress and Future Prospectives. *Recent Pat. Antiinfect. Drug Discov.* **2012**, *7*, 28–35, https://doi.org/10.2174/157489112799829684.
15. Burt, S. Essential oils: their antibacterial properties and potential applications in foods—a review. *Int. J. Food Microbiol.* **2004**, *94*, 223–253, https://doi.org/10.1016/j.ijfoodmicro.2004.03.022.
16. Hyldgaard, M.; Mygind, T.; Meyer, R.L. Essential Oils in Food Preservation: Mode of Action, Synergies, and Interactions with Food Matrix Components. *Front. Microbiol.* **2012**, *3*, 12, https://doi.org/10.3389/fmicb.2012.00012.
17. Di Pasqua, R.; Betts, G.; Hoskins, N.; Edwards, M.; Ercolini, D.; Mauriello, G. Membrane Toxicity of Antimicrobial Compounds from Essential Oils. *J. Agric. Food Chem.* **2007**, *55*, 4863-4870, https://doi.org/10.1021/jf0636465.
18. Dembińska, K.; Shinde, A.H.; Pejchalová, M.; Richert, A.; Swiontek Brzezinska, M. The Application of Natural Phenolic Substances as Antimicrobial Agents in Agriculture and Food Industry. *Foods* **2025**, *14*, 1893, https://doi.org/10.3390/foods14111893.
19. Kowalewska, A.; Majewska-Smolarek, K. Eugenol-Based Polymeric Materials—Antibacterial Activity and Applications. *Antibiotics* **2023**, *12*, 1570, https://doi.org/10.3390/antibiotics12111570.
20. Iskandar, K.; Ahmed, N.; Paudyal, N.; Ruiz Alvarez, M.-J.; Balasubramani, S.P.; Saadeh, D.; Ullah Baig, S.; Sami, H.; Hammoudi Halat, D.; Pavlović, N.; Roques, C.; Rizvi, M.; Salameh, P.; Hamed, F.; Van

Dongen, M. Essential Oils as Antimicrobial Agents Against WHO Priority Bacterial Pathogens: A Strategic Review of In Vitro Clinical Efficacy, Innovations and Research Gaps. *Antibiotics* **2025**, *14*, 1250, https://doi.org/10.3390/antibiotics14121250.

21. Kitchen, D.B.; Decornez, H.; Furr, J.R.; Bajorath, J. Docking and scoring in virtual screening for drug discovery: methods and applications. *Nat. Rev. Drug Discov.* **2004**, *3*, 935–949, https://doi.org/10.1038/nrd1549.
22. Ferreira, L.G.; Dos Santos, R.N.; Oliva, G.; Andricopulo, A.D. Molecular Docking and Structure-Based Drug Design Strategies. *Molecules* **2015**, *20*, 13384-13421, https://doi.org/10.3390/molecules200713384.
23. Pagadala, N.S.; Syed, K.; Tuszynski, J. Software for molecular docking: a review. *Biophys. Rev.* **2017**, *9*, 91-102, https://doi.org/10.1007/s12551-016-0247-1.
24. Evanthia, L.; George, S.; Demetrios, K.V.; Zoe, C. Structure-Based Virtual Screening for Drug Discovery: Principles, Applications and Recent Advances. *Curr. Top. Med. Chem.* **2014**, *14*, 1923-1938, https://doi.org/10.2174/1568026614666140929124445.
25. Hsu, K.-C.; Chen, Y.-F.; Lin, S.-R.; Yang, J.-M. iGEMDOCK: a graphical environment of enhancing GEMDOCK using pharmacological interactions and post-screening analysis. *BMC Bioinformatics* **2011**, *12*, S33, https://doi.org/10.1186/1471-2105-12-S1-S33.
26. Krieger, E.; Vriend, G. YASARA View—molecular graphics for all devices—from smartphones to workstations. *Bioinformatics* **2014**, *30*, 2981-2982, https://doi.org/10.1093/bioinformatics/btu426.
27. Daina, A.; Michielin, O.; Zoete, V. SwissADME: a free web tool to evaluate pharmacokinetics, drug-likeness and medicinal chemistry friendliness of small molecules. *Sci. Rep.* **2017**, *7*, 42717, https://doi.org/10.1038/srep42717.
28. van de Waterbeemd, H.; Gifford, E. ADMET *in silico* modelling: towards prediction paradise? *Nat. Rev. Drug Discov.* **2003**, *2*, 192–204, https://doi.org/10.1038/nrd1032.
29. Gleeson, M.P.; Hersey, A.; Hannongbua, S. In-Silico ADME Models: A General Assessment of their Utility in Drug Discovery Applications. *Curr. Top. Med. Chem.* **2011**, *11*, 358–381, https://doi.org/10.2174/156802611794480927.
30. Toutain, P.-L.; Pelligand, L.; Lees, P.; Bousquet-Mélou, A.; Ferran, A.A.; Turnidge, J.D. The pharmacokinetic/pharmacodynamic paradigm for antimicrobial drugs in veterinary medicine: Recent advances and critical appraisal. *J. Vet. Pharmacol. Ther.* **2021**, *44*, 172-200, https://doi.org/10.1111/jvp.12917.
31. Toutain, P.-L.; Ferran, A.; Bousquet-Mélou, A. Species Differences in Pharmacokinetics and Pharmacodynamics. In Comparative and Veterinary Pharmacology, Cunningham, F., Elliott, J., Lees, P., Eds.; Springer Berlin Heidelberg: Berlin, Heidelberg, **2010**; Volume 199, pp. 19-48, https://doi.org/10.1007/978-3-642-10324-7_2.
32. Hariharan H. Antimicrobial Therapy in Veterinary Medicine, 4th ed. Can Vet J. 2007 Jul;48(7):744. PMCID: PMC1899851.
33. Shoichet, B.K. Virtual screening of chemical libraries. *Nature* **2004**, *432*, 862–865, https://doi.org/10.1038/nature03197.
34. Cheng, T.; Li, X.; Li, Y.; Liu, Z.; Wang, R. Comparative Assessment of Scoring Functions on a Diverse Test Set. *J. Chem. Inf. Model.* **2009**, *49*, 1079-1093, https://doi.org/10.1021/ci9000053.
35. Scior, T.; Bender, A.; Tresadern, G.; Medina-Franco, J.L.; Martínez-Mayorga, K.; Langer, T.; Cuanalo-Contreras, K.; Agrafiotis, D.K. Recognizing Pitfalls in Virtual Screening: A Critical Review. *J. Chem. Inf. Model.* **2012**, *52*, 867-881, https://doi.org/10.1021/ci200528d.
36. Ekins, S.; Mestres, J.; Testa, B. *In silico* pharmacology for drug discovery: applications to targets and beyond. *Br. J. Pharmacol.* **2007**, *152*, 21–37, https://doi.org/10.1038/sj.bjp.0707306.
37. Lu, J.; Patel, S.; Sharma, N.; Soisson, S.M.; Kishii, R.; Takei, M.; Fukuda, Y.; Lumb, K.J.; Singh, S.B. Structures of Kibdelomycin Bound to *Staphylococcus aureus* GyrB and ParE Showed a Novel U-Shaped Binding Mode. *ACS Chem. Biol.* **2014**, *9*, 2023-2031, https://doi.org/10.1021/cb5001197.
38. Rajakumari, K.; Aravind, K.; Balamugundhan, M.; Jagadeesan, M.; Somasundaram, A.; Brindha Devi, P.; Ramasamy, P. Comprehensive review of DNA gyrase as enzymatic target for drug discovery and development. *Eur. J. Med. Chem. Rep.* **2024**, *12*, 100233, https://doi.org/10.1016/j.ejmcr.2024.100233.
39. Sofi, F.A.; Mayank; Masoodi, M.H.; Tabassum, N. Recent advancements in the development of next-generation dual-targeting antibacterial agents. *RSC Med. Chem.* **2025**, *16*, 1891-1922, https://doi.org/10.1039/D4MD00934G.

40. Poonam, P.; Ajay, K.; Akanksha, K.; Tamanna, V.; Vritti, P. Recent Development of DNA Gyrase Inhibitors: An Update. *Mini-Rev. Med. Chem.* **2024**, *24*, 1001-1030, https://doi.org/10.2174/0113895575264264230921080718.
41. Cotman, A.E.; Fulgheri, F.; Piga, M.; Peršolja, P.; Tiz, D.B.; Skok, Ž.; Durcik, M.; Sterle, M.; Dernovšek, J.; Cruz, C.D.; Tammela, P.; Szili, P.É.; Daruka, L.; Pál, C.; Zega, A.; Mašič, L.P.; Ilaš, J.; Tomašič, T.; Kikelj, D.; Zidar, N. New *N*-phenylpyrrolamide inhibitors of DNA gyrase with improved antibacterial activity. *RSC Adv.* **2024**, *14*, 28423-28454, https://doi.org/10.1039/D4RA04802D.
42. Leyn SA, Kent JE, Zlamal JE, Elane ML, Vercruysse M, Osterman AL. Two Classes of DNA Gyrase Inhibitors Elicit Distinct Evolutionary Trajectories Toward Resistance in Gram-Negative Pathogens. bioRxiv [Preprint]. 2023 Sep 21:2023.06.26.546596. doi: 10.1101/2023.06.26.546596. Update in: NPJ Antimicrob Resist. 2024 Mar 2;2(1):5. doi: 10.1038/s44259-024-00021-y. PMID: 37425702; PMCID: PMC10327078.
43. Vittorio S, Lunghini F, Morerio P, Gadioli D, Orlandini S, Silva P, Jan Martinovic, Pedretti A, Bonanni D, Del Bue A, Palermo G, Vistoli G, Beccari AR. Addressing docking pose selection with structure-based deep learning: Recent advances, challenges and opportunities. Comput Struct Biotechnol J. 2024 May 18;23:2141-2151. doi: 10.1016/j.csbj.2024.05.024. Erratum in: Comput Struct Biotechnol J. 2024 Jul 17;23:2963. doi: 10.1016/j.csbj.2024.07.001. PMID: 38827235; PMCID: PMC11141151.
44. Nivatya, H.K.; Singh, A.; Kumar, N.; Sonam; Sharma, L.; Singh, V.; Mishra, R.; Gaur, N.; Mishra, A.K. Assessing molecular docking tools: understanding drug discovery and design. *Futur. J. Pharm. Sci.* **2025**, *11*, 111, https://doi.org/10.1186/s43094-025-00862-y.
45. Kim, H.; Shim, H.; Ranganath, A.; He, S.; Stevenson, G.; Allen, J.E. Protein-ligand binding affinity prediction using multi-instance learning with docking structures. *Front. Pharmacol.* **2025**, *15*, 1518875, https://doi.org/10.3389/fphar.2024.1518875.
46. Elsaman, T.; Mohamed, M.A.; Mohamed, M.S.; Eltayib, E.M.; Abdalla, A.E. Microbial-based natural products as potential inhibitors targeting DNA gyrase B of *Mycobacterium tuberculosis*: an *in silico* study. *Front. Chem.* **2025**, *13*, 1524607, https://doi.org/10.3389/fchem.2025.1524607.
47. Moon, S.; Zhung, W.; Kim, W.Y. Toward generalizable structure-based deep learning models for protein–ligand interaction prediction: Challenges and strategies. *WIREs Comput. Mol. Sci.* **2024**, *14*, e1705, https://doi.org/10.1002/wcms.1705.

Publisher's Note & Disclaimer

Supplementary Material

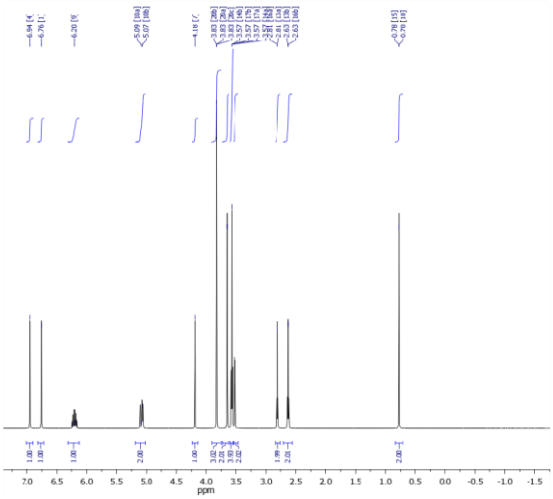

Figure S1. ^{1}H NMR spectrum of the studied compound (L1) recorded at 300 MHz in DMSO. Chemical shifts (δ) are reported in ppm relative to the residual solvent peak, with signal multiplicities and integrals indicated, confirming the proposed molecular structure.

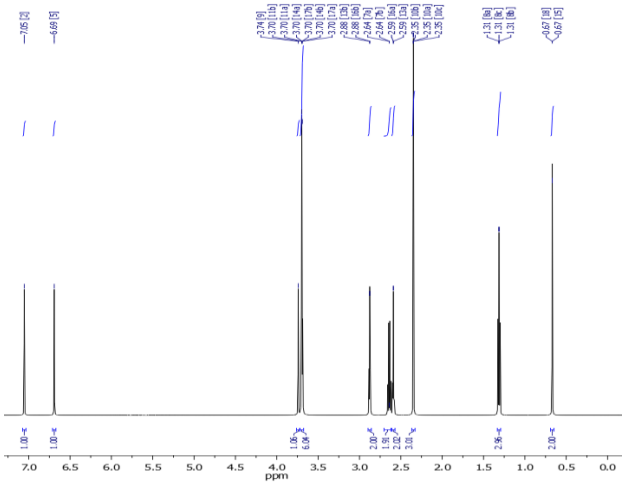

Figure S2. ^{1}H NMR spectrum of the studied compound (L2) recorded at 300 MHz in DMSO. Chemical shifts (*δ*) are reported in ppm relative to the residual solvent peak, with signal multiplicities and integrals indicated, confirming the proposed molecular structure.

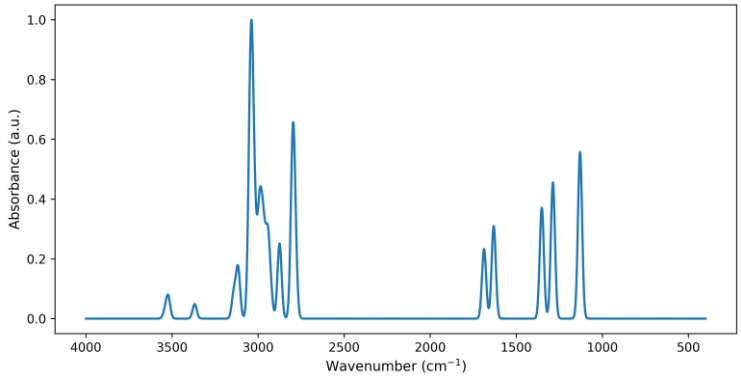

Figure S3. Infrared (IR) spectrum (L1). The spectrum was generated by Gaussian convolution of the vibrational modes (σ = 12 cm^{-1}) and normalized to the most intense band.

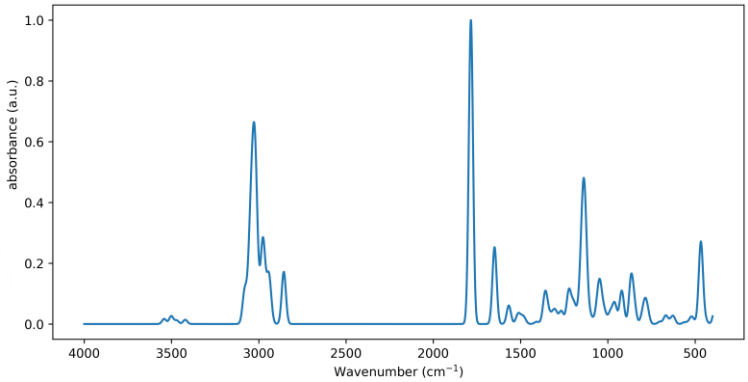

Figure S4. Infrared (IR) spectrum (L2). The spectrum was generated by Gaussian convolution of the vibrational modes (σ = 12 cm^{-1}) and normalized to the most intense band.